Immobilizing Redox-Active Tricycloquinazoline into a 2D Conductive Metal–Organic Framework for Lithium Storage

Jie Yan, Yutao Cui, Mo Xie, Guo-Zhan Yang, De-Shan Bin,* and Dan Li*

Abstract: *Heteroaromatic-conjugated aromatic molecules have inspired numerous interests in rechargeable batteries like Li-ion batteries, but were limited by low conductivity and easy dissolution in electrolytes. Herein, we immobilize a nitrogen-rich aromatic molecule tricycloquinazoline (TQ) and CuO_4 unit into a two-dimensional (2D) conductive metal–organic framework (MOF) to unlock their potential for Li^+ storage. TQ was identified redox activity with Li^+ for the first time. With a synergistic effect of TQ and CuO_4 unit, the 2D conductive MOF, named Cu-HHTQ (HHTQ = 2,3,7,8,12,13-hexahydroxytricycloquinazoline), can facilitate the Li^+/e^- transport and ensure a resilient electrode, resulting in a high capacity of 657.6 $mAh\,g^{-1}$ at 600 $mA\,g^{-1}$ with extraordinary high-rate capability and impressive cyclability. Our findings highlight an efficient strategy of constructing electrode materials for energy storage with combining multiple redox-active moieties into conductive MOFs.*

Lithium-ion batteries (LIBs) have drawn great attentions for various applications such as portable devices, electric vehicles and smart grid.[1] Therefore, numerous research efforts have been devoted to the development of advanced electrode materials for Li^+ storage with an overall consideration of the electrochemical performance, resource sustainability and environmental benignity.[2] Owing to their abundant resource, environmental friendliness, flexible structure designability and high theoretical capacity, organic electrode materials have inspired numerous interests in LIBs.[3] Among various organic electrode materials, heteroaromatic-conjugated aromatic molecules with multi-electron redox activity for Li^+ storage[4] originated from the redox-active group like C=N,[5] C≡N,[6] and N=N[7] can ensure a high specific capacity, thus they are now drawing increasing research interest for high-energy-density LIBs electrodes.[8] Despite their advantages, the development of organic electrodes based on heteroaromatic-conjugated aromatic molecules is challenged by their easy dissolution in organic electrolytes, low electronic conductivity and sluggish reaction kinetics.[9] Building such redox-active molecules into polymeric structures, like

metal–organic frameworks (MOFs) which are constructed by functional molecular building blocks and metal nodes,[10] have witnessed numerous successes in resisting the solubility in organic electrolytes to ensure a robust electrode.[11] However, traditional MOFs show low electrical conductivity, which locks their potential for electrochemical energy storage. Two-dimensional (2D) conductive MOFs featured in-plane π-conjugation structure are a type of multifunctional materials exhibiting outstanding electrical conductivity, usually constructed from aromatic ligands with ortho-substituted donor atoms (O, N, S or Se) and single metal ions with square-planar coordinative geometry.[12] The rigidity of 2D conductive MOFs resists their solubility in organic electrolytes for outstanding cyclability, and the good conductivity together with built-in micropores would facilitate the transmission of both ions and electrons to ensure high-rate capability. Conductive MOFs have shown great potential in electrochemical applications.[11c,13] Up to now, the redox activity of conductive MOFs as electrode materials mainly results from donor atoms (X) in the aromatic ligands and metal centers (M), namely the coordination units of MX_4.[14] Heteroaromatic π-conjugated aromatic compounds with different donor atoms as organic ligands in 2D conductive MOFs are rarely reported.[15]

As bottom-up fabricated materials, 2D conductive MOFs provide an effective platform for immobilizing redox-active organic molecules into a resilient electrode with improved electrochemical performance for applications in lithium storage. Among various heteroaromatic-conjugated aromatic molecules, a nitrogen-rich aromatic molecule tricycloquinazoline (TQ) is suitable for the construction of electrode materials, initially sparked by the existence of four nitrogen atoms with large π- conjugation in the molecule, where C=N bond has a rich electron density to facilitate Li^+ ions gathering and serve as electrochemical reaction centers.[5,11b,16] In addition, each aromatic C_6 ring was proved to accept one Li^+ ion to form an inserted Li/C_6.[17] Therefore, it is expected that two reversible three-electron oxidations undergo on the central N-doped phenalene of TQ and one reversible three-electron oxidations undergo on the three terminal phenyl rings (Scheme 1a).

We thus hypothesize that there are nine-electron related redox-active behavior of TQ for Li^+ storage. With nine Li^+ ions loaded, the calculated theoretical specific capacity of TQ can reach 752.9 $mAh\,g^{-1}$, which is among one of the highest capacities in organic electrode materials.[3b,d] The excellent redox activity and high C_3 symmetry make TQ to be potential organic building block of robust frameworks for electrochemical applications.

[*] Dr. J. Yan, Dr. Y. Cui, Dr. M. Xie, G. Yang, Prof. Dr. D. Bin,
Prof. Dr. D. Li
College of Chemistry and Materials Science, and Guangdong
Provincial Key Laboratory of Functional Supramolecular Coordination
Materials and Applications, Jinan University
Guangzhou 510632 (P. R. China)
E-mail: bindeshan@jnu.edu.cn
danli@jnu.edu.cn

Supporting information and the ORCID identification number(s) for
the author(s) of this article can be found under:
https://doi.org/10.1002/anie.202110373.
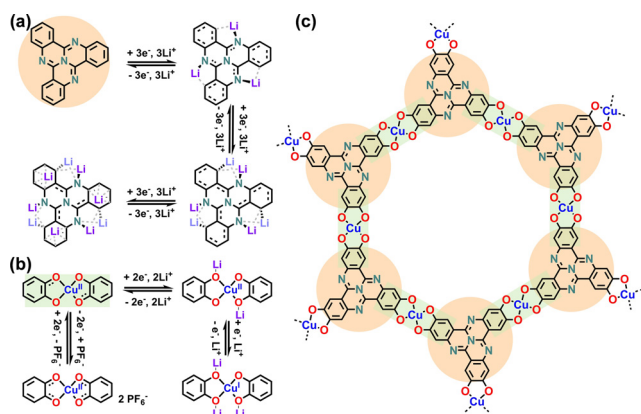
Scheme 1. a) The predicted reversible reaction mechanism of TQ for energy storage. b) The reversible reaction mechanism of CuO$_4$ unit for energy storage. c) Chemical structure of Cu-HHTQ.

The CuO$_4$ unit, originated from the dioxolene ligands and the metal Cu, have recently been identified as promising redox-active unit for Li$^+$ ion storage (Scheme 1 b).[11c,18] Each dioxolene ligand was found to undergo two reversible one-electron oxidations to give redox series of catechol, semi-quinone and quinone (Figure S6), while the metal Cu has one reversible one-electron oxidation to generate species Cu^{II} and Cu^I.[11c] So the CuO$_4$ unit can undergo 5-electron redox-active reaction. Considering the probable excellent redox activity of TQ and CuO$_4$ unit, herein we devoted our efforts to immobilize the TQ molecule and CuO$_4$ metal node into a 2D conductive MOF named Cu-HHTQ (HHTQ = 2,3,7,8,12,13-hexahydroxytricycloquinazoline) for high-performance Li$^+$ storage (Scheme 1 c). As a novel redox-active molecule, TQ was identified nine-electron redox activity with Li$^+$ through experimental results and theoretical calculations for the first time. With rigid and continuous framework, Cu-HHTQ electrode exhibits promising electrochemical perfor-

mance exemplified by the extraordinary reversible capacity (657.6 mAh g^{-1} at 600 mA g^{-1}), high-rate capability (292 mAh g^{-1} at 3000 mA g^{-1}) and impressive cyclability (82% capacity retention after 200 cycling). As a novel redox-active molecule, TQ exhibits great potential as organic building blocks for the construction of electrochemical active materials. With combining multiple redox-active moieties into conductive MOFs, our findings highlight an efficient strategy of discovering electrode materials for energy storage.

The 2D conductive MOF Cu-HHTQ was synthesized solvothermally in a mixed solvent of N,N-dimethylformamide (DMF) and water at 85 °C for 24 h (Figure 1 a).[15] As showed in Figure 1 b, HHTQ linkers organized with copper ions, forming a crystalline Cu-HHTQ with a 2D honeycomb structure. The powder X-ray diffraction (PXRD) results reveal good crystallinity and long-range order of Cu-HHTQ. The dominant peaks at 4.0°, 8.0°, 10.6° and 13.9°, according to [100], [200], [210] and [220] reflections, indicate long-range order within the *ab* plane. The position and intensity of the diffraction peaks are well consistent with the reported 2D honeycomb lattice of Cu-HHTQ with eclipsed (AA) staking pattern.[15,19] A 2D hexagonal lattice with AA staking patterns (cell parameter: $a = b = 25.41$ Å, $c = 3.19$ Å, $\alpha = \beta = 90$, $\gamma = 120°$ in $P\bar{6}2m$ space group) was simulated accordingly. The distinct peak at 27.6° is according to [001] reflections and indicates an interlayer distance of ≈3.2 Å. The PXRD pattern can be well reproduced with the simulated lattice as negligible difference was shown in Pawley refinement (Rwp = 2.67%, Rp = 2.03%). (Figure 1 c) The visible lattice fringe conducted by high-resolution transmission electron microscopy (HRTEM) further confirmed the long-range ordered crystalline structure of Cu-HHTQ (Figure 1 d–g, Figure S7). The amplifying HRTEM image (Figure 1 e) indicates that the hexagonal pore size of Cu-HHTQ is about 2.52 nm, which is greatly appropriate with the anticipated structure. In accordance with the calculated patterns, HRTEM of Cu-HHTQ
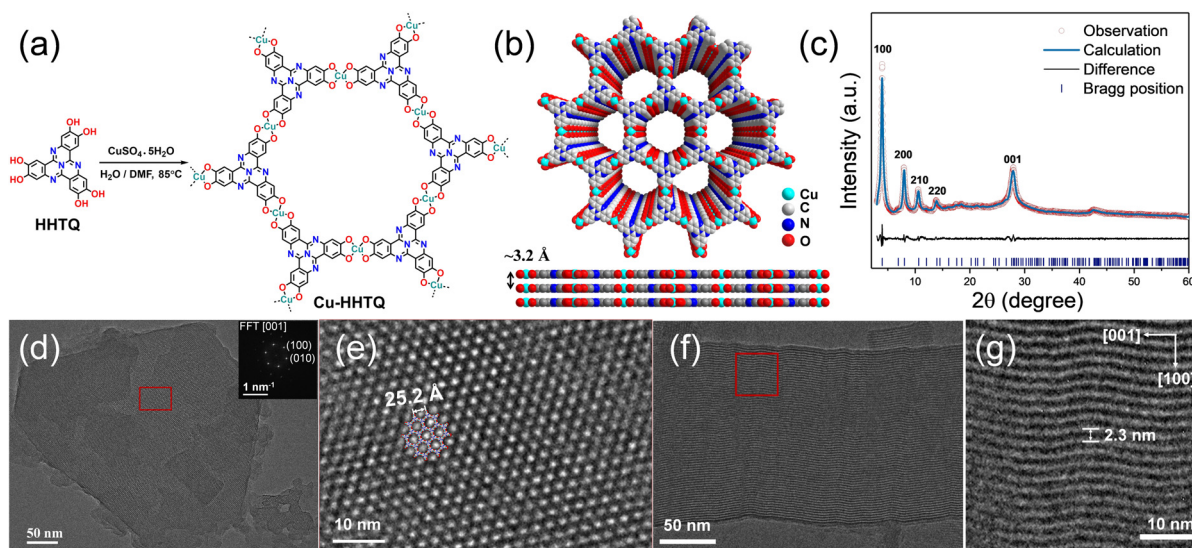

Figure 1. a) Synthesis of Cu-HHTQ. b) The calculated structure of Cu-HHTQ. c) Pawley refined and experimental PXRD patterns of Cu-HHTQ. d) HRTEM and fast Fourier transform (FFT) image (insert) of Cu-HHTQ along *c* direction. e) Enlarged image of selected section in (d). f) HRTEM of Cu-HHTQ perpendicular to [001] direction. g) Enlarged image of selected section in (f).

perpendicular to [001] direction shows the distance between the layers to be $d_{100} = 2.3$ nm. The porosity was confirmed by the N_2 adsorption isotherm with Brunauer-Emmett-Teller (BET) surface area of 516.99 m^2g^{-1} (Figure S8).

The energy dispersive spectroscopy (EDS) spectra provided that C, N, O and Cu elements were uniformly distributed on the Cu-HHTQ (Figure S9). The elemental contents were further confirmed by the X-ray photoelectron spectroscopy (XPS) spectrum (Figure S10). The satellite peaks in high-resolution Cu 2p spectra represent that the copper ion in the +2-oxidation state.[20] The two peaks with binding energies of 933.2 and 935.6 eV are correspond to Cu $2p_{3/2}$, indicating the existence of two kinds of Cu^{II} in different chemistry environment. The weaker peak might originate from Cu^{II} located at the edge of the 2D Cu-HHTQ layer or the surface of the nanocrystals. The morphology of Cu-HHTQ was observed by scanning electron microscopy (SEM), which shows apparently layer structures of stacked 2D flakes (Figure S11). The electrical conductivity of Cu-HHTQ was measured on pressed pellets through standard four-probe method. The temperature-dependent conductivity revealed a semi-conductive behavior of Cu-HHTQ (Figure S12). The electrical conductivity of Cu-HHTQ reaches 5×10^{-3} S cm^{-1} at 298 K and increases to be 2.6×10^{-2} S cm^{-1} at 400 K. The optical band gap of 1.18 eV extracted from UV-visible spectrum (Figure S13) also proves the semi-conductive behavior of Cu-HHTQ. Besides, both thermal stability and chemical stability of Cu-HHTQ were estimated. The thermogravimetric analysis (TGA) curve of Cu-HHTQ shows good thermal stability under 280°C (Figure S14). The PXRD patterns of Cu-HHTQ well maintains with the pristine ones after immersing into 1 M NaOH and 1 M $LiPF_6$ (Figure S15), revealing its good chemical stability.

Attributed to the excellent structural features as mentioned above, Cu-HHTQ can be supposed to have significant implications and applications in LIBs. The repeat unit $Cu_{1.5}HHTQ$ of Cu-HHTQ, containing one TQ and 1.5 CuO_4 units, was identified 16.5-electron redox activity with Li$^+$. And the calculated theoretical specific capacity of Cu-HHTQ with 16.5-electron redox activity can reach 874.6 mAh g^{-1}. Cu-HHTQ was then applied as active material for Li$^+$ storage with Li metal as counter electrode in a half-cell configuration and the charge/discharge tests were performed in a voltage range of 0.01 to 3.0 V (vs. Li$^+$/Li). The charge and discharge profiles in the first three cycles of Cu-HHTQ at 15 mA g^{-1} were pictured in Figure 2a. In the first cycle, discharge and charge capacities of Cu-HHTQ were 1716 and 989 mAh g^{-1}, respectively. The capacity of 989 mAh g^{-1} is among one of the highest values in reported conductive MOFs (Table S1). The most probable causes of the extra capacity of Cu-HHTQ may be the interfacial charge storage, the formation/decomposition of electrolyte-derived surface layer and surface reaction.[21] The charged capacity of Cu-HHTQ for the second cycle is 828 mAh g^{-1}, which is consistent with the theoretical capacity. Cycling performance of Cu-HHTQ was firstly performed at 300 mA g^{-1} for 50 cycles (Figure S16) and then 600 mA g^{-1} for another 200 cycles (Figure 2b). The capacity of Cu-HHTQ decreased in the first 15 cycles and then increased, which is possibly resulting from the sufficient
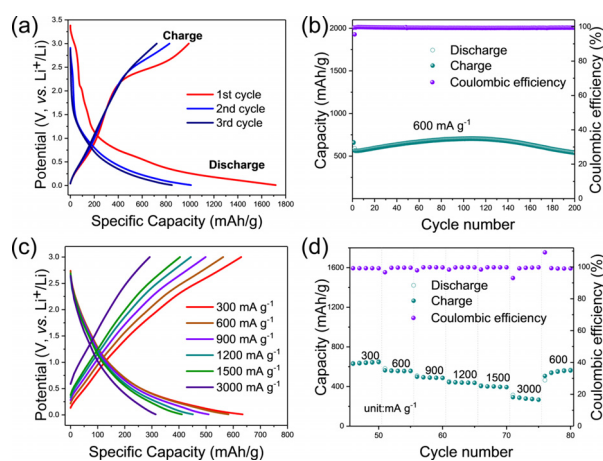
Figure 2. a) Charge and discharge profiles of Cu-HHTQ at 15 mA g^{-1} in the first three cycles. b) Cycling performance of Cu-HHTQ at 600 mA g^{-1}. c) Charge and discharge curves of Cu-HHTQ at various current densities. (d) Rate performance of Cu-HHTQ at various current densities from 300 to 3000 mA g^{-1}.

permeation of electrolyte for electrode after several cycles[22] and the activated process of the highly crystalline MOF.[11c,23] During the cycling, Cu-HHTQ could deliver a capacity of 657.6 mAh g^{-1} at 600 mA g^{-1} and a capacity retention of 82% after 200 cycles. Only slight capacity decay of 0.09% per cycle was observed with a high Coulombic efficiency around 99.5% during the cycling. After 250 cycles, the capacity retention reaches $\approx 73\%$. (Figure S17) Rate performance of Cu-HHTQ (Figure 2c and Figure 2d) was conducted at various current densities after 50 cycles at 300 mA g^{-1} because of the activated process. At different high current densities of 1200, 1500, 3000 mA g^{-1}, the Cu-HHTQ exhibits high capacities of 443.7, 403.7, 292.1 mAh g^{-1}, respectively, indicating good rate performance of Cu-HHTQ. The conductivity and porosity of Cu-HHTQ might benefit the fast transmission of ion and electron,[24] resulting in good rate performance. The rate performance of Cu-HHTQ was also conducted in the first 30 cycles at different current densities varied from 30 to 1500 mA g^{-1} (Figure S18). The capacity of Cu-HHTQ slightly declines at high current densities, showing good rate performance similarly. The charge/discharge tests were also conducted in a voltage range of 0.01 to 2.5 V (vs. Li$^+$/Li, Figure S19). A reversible capacity of 404.8 mAh g^{-1} at 300 mA g^{-1} over 200 cycles is achieved, which is also among the high values in organic electrode materials.

CV measurements were carried out with various scan rates to understand the charge-storage mechanism of Cu-HHTQ (Figure S20 and S21). Partly capacitive charge storage in Cu-HHTQ can be confirmed (detail in SI) and the capacitive contributions were calculated to be 39% to 58% at the scan rates varied from 0.2 to 1.0 mV s^{-1}. The high conductivity, large specific surface area and continuous pores, combined with the multiple redox-activity in Cu-HHTQ endowed the anode a high capacitive contribution. It is noted that designing anode materials with high capacitive contribution has been recognized as an effective strategy to build high-rate anode for LIBs and beyond.[25] Immobilizing the functional organic ligand into conductive MOF with appropriate
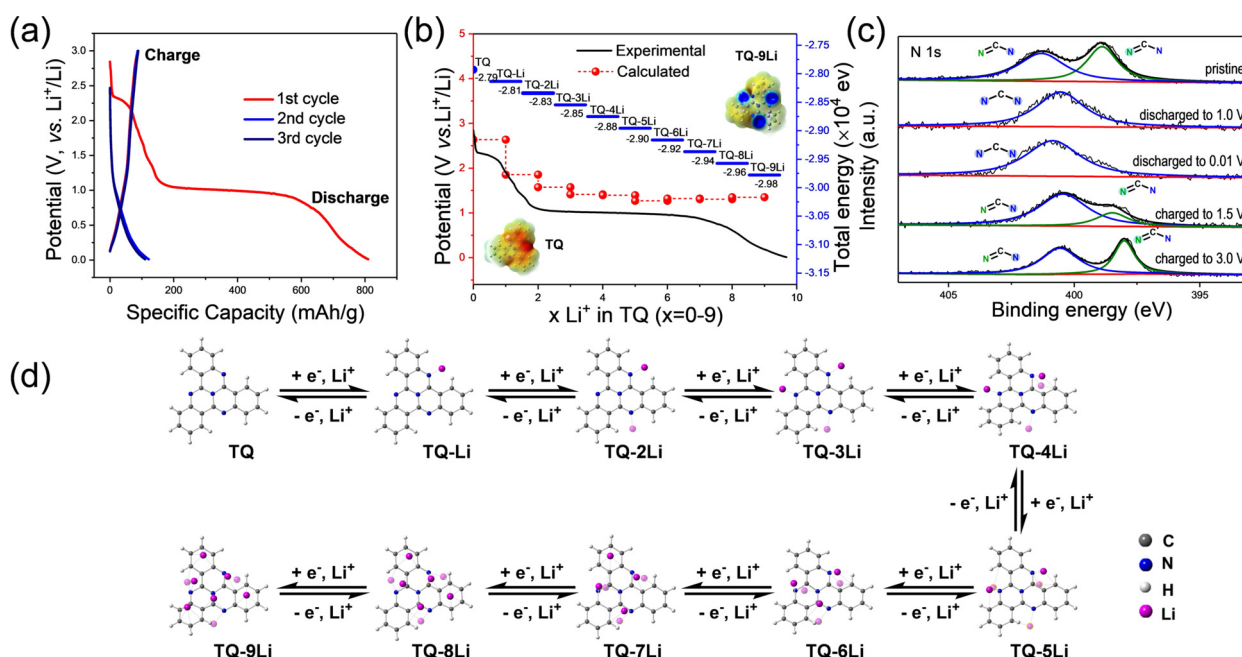
Figure 3. a) Charge and discharge profiles of TQ at 30 mAg^{-1} in the first three cycles. b) Experimental (black line) and calculated (red dotted lines) voltage profiles (left axis) of TQ at the potential range between 0.01 and 3.0 V (vs. Li$^+$/Li). The right axis shows the total energy of different lithiation structures of TQ (in blue). Insert: ESP images of TQ and TQ-9Li. c) Ex situ XPS N 1s spectra of TQ at different charged and discharged states. d) Structure evolution of TQ lithiation pathway in LIBs calculated by DFT.

specific surface area and pore size and sufficient redox-active sites could be an effective strategy to facilitate both capacitive contribution and diffusion contribution, resulting in the high-performance electrode materials.

Cu-HHTQ electrode exhibits prominent capacity in lithium storage. As hypothesized above, we attributed the excellent redox performance of Cu-HHTQ to a synergy of TQ and CuO$_4$ unit. To verify the redox activity of TQ, TQ was synthesized[26] and applied as active material with Li metal as counter electrode (Figure 3 and Figure S22–S26). Figure 3a illustrates the charge and discharge profiles in the first three cycles of TQ at 30 mAg^{-1}. In the first cycle, the discharge and charge capacities of TQ were 810 and 88.3 mAhg^{-1}, respectively, resulting in an initial Coulombic efficiency of 10.9%. The high discharge capacity of the first cycle reveals the excellent redox-activity of TQ. The low value for the reversible capacities might attribute to the solubility of TQ into the electrolyte. The cyclic voltammogram (CV) test of TQ was performed in the potential range of 0.01 to 3.0 V with a scan rate of 0.1 mVs^{-1}. (Figure S22) The broad reductive and oxidative peaks at 0.9 and 1.1 V are related to the combined redox behavior of TQ. The sloping discharge plateaus (Figure 3a) presented at 1.0 V are consistent with the CV results. The broad reductive/oxidative peaks at about 0.5 V in the CV curve of Cu-HHTQ (Figure S20) result from the combined redox behavior of organic ligands. Compared to TQ, the lower potential of the reductive/oxidative peaks can attribute to the substitution of TQ by strong electron-donating O. The broad reductive/oxidative peaks at about 2.5 V might assign to the combined redox behavior of Cu. The multiple redox-active sites including TQ, ortho-substituted O and Cu endow Cu-HHTQ with complex redox-activity. And

the extended π conjugated structure of Cu-HHTQ might also result in different redox behavior from the isolated aromatic TQ.

To further understand the lithium storage mechanism of TQ, we calculated the electrostatic potentials (ESP), the thermodynamic energies, and voltage changes of TQ and TQ-xLi structures. Based on the TQ structure, around the electrostatic potential minima point was considered to predict the possible lithium binding positions.[27] The calculation results revealed that nine electrons could be bound with TQ during the discharge and charge process, in good agreement with our earlier speculation. The structure evolution from TQ to TQ-9Li was illustrated in Figure 3d and Figure S27. The total energy with the structure evolution of TQ-xLi and binding energy of the lithiation of TQ were shown in Figure S28 and Table S2. As shown in the ESP diagrams, the negative electrostatic potential is around the pyrimidine nitrogen atoms. Firstly, one Li$^+$ ion binds with the pyrimidine N atom to form TQ-Li. Then the second and third Li$^+$ ions bind with another two pyrimidine N atom to form TQ-2Li and TQ-3Li. The fourth, fifth and sixth Li$^+$ ions locate around the central N atom and C=C bonds adjacent to the C=N bonds by electrostatic interactions, and distribute at alternating sides of the TQ plane together with the first three Li$^+$ ions. After six Li atoms inserted, the electrostatic potential of the terminal phenyl rings shows relatively negative. And the seventh, eighth and nineth Li$^+$ ions bind with the terminal three phenyl rings separately. Figure 3b shows the experimental and calculated potentials in the discharge process at a potential window of 0.01–3.0 V. As calculated, when the first Li$^+$ ion was loaded into the structure of TQ, the voltage comes to 2.64 V and the voltage comes to 1.35 V when loaded with nine

Li$^+$ ions, corresponding to the voltages of the reduction peak in the CV diagram (Figure S22). The trend of voltage decrease of calculated results was in good agreement with the experimental phenomenon.

To study the electrochemical redox process, the structure changes of TQ were further tested by an ex situ XPS characterization. The high-resolution spectrum of N 1s (Figure 3c) indicates two kinds of N, namely C=N peak at 398.9 eV and C-N peak at 401.3 eV in the pristine state. During the discharge process, C=N peak completely vanished and transformed to C-N peak. Upon fully charged, the C=N peak and C-N peak recovered back to the pristine state, showing good reversibility. The experimental results proved that the functional group pyrimidine undergo the redox process at the N-doped phenalene. The experimental results observed by the ex situ XPS are in high accordance with the calculated results of TQ structure evolution.

The chemical states of Cu-HHTQ were also investigated by ex situ XPS during the charge and discharge process. As shown in the high-resolution XPS N 1s spectra of Cu-HHTQ (Figure S29), the strength of C=N peak decreased and the strength of C-N increased after discharging process. After the charging process, the strength of C=N recovered back and the strength of C-N decreased, indicating that redox-active reaction occurred in the pyrimidine N atoms with good reversibility. As shown in the high-resolution of Cu 2P$_{3/2}$ spectra (Figure S30-S32), the two peaks of Cu^{II} assigned to 933.6 and 936.1 eV in pristine state disappeared after fully discharged to 0.01 V and Cu^{I} peak assigned to 933.5 eV arise, indicating the fully reduction of Cu^{II} to Cu^{I}. After charged to 3.0 V, the strength of Cu^{II} peaks recovered and the Cu^{I} peak disappeared. The obvious transformation of Cu^{II} to Cu^{I} indicates that the redox reactions are partly attributed to Cu atom in the discharge and charge process. The experimental results prove that both TQ and CuO$_4$ units in Cu-HHTQ undergo the redox process.

In summary, a nitrogen-rich aromatic molecule TQ and a TQ-based conductive MOF Cu-HHTQ integrated with redox CuO$_4$ units were synthesized and well-explored as electrode materials for lithium storage. The redox activity of TQ was confirmed by both experimental results and theoretical calculations. To the best of our knowledge, this is the first time that TQ was identified redox activity and researched as electrode material for lithium storage. The TQ-based 2D conductive MOF Cu-HHTQ exhibits excellent specific capacity with 657.6 mAh g^{-1} at 600 mA g^{-1} and a capacity retention of 82% after 200 cycles. It is among one of the highest specific capacities in reported conductive MOFs. Further researches on design and synthesis of organic electrode materials based on the novel redox-active TQ for energy storage are worth pursuing. We expect our findings shed light on assembling multiple redox-active organic moieties into high-performance electrodes enabled by a reticular-chemistry strategy.

Conflict of Interest

The authors declare no conflict of interest.

[1] a) E. Fan, L. Li, Z. Wang, J. Lin, Y. Huang, Y. Yao, R. Chen, F. Wu, *Chem. Rev.* **2020**, *120*, 7020–7063; b) B. Dunn, H. Kamath, J.-M. Tarascon, *Science* **2011**, *334*, 928–935; c) E. Pomerantseva, F. Bonaccorso, X. Feng, Y. Cui, Y. Gogotsi, *Science* **2019**, *366*, eaan8285; d) J. Liu, Z. Bao, Y. Cui, E. J. Dufek, J. B. Goodenough, P. Khalifah, Q. Li, B. Y. Liaw, P. Liu, A. Manthiram, Y. S. Meng, V. R. Subramanian, M. F. Toney, V. V. Viswanathan, M. S. Whittingham, J. Xiao, W. Xu, J. Yang, X. Yang, J. Zhang, *Nat. Energy* **2019**, *4*, 180–186.

[2] Y. Liu, Y. Zhu, Y. Cui, *Nat. Energy* **2019**, *4*, 540–550.

[3] a) Y. Chen, C. Wang, *Acc. Chem. Res.* **2020**, *53*, 2636–2647; b) Y. Lu, J. Chen, *Nat. Rev. Chem.* **2020**, *4*, 127–142; c) W. Zhang, W. Huang, Q. Zhang, *Chem. Eur. J.* **2021**, *27*, 6131–6144; d) D. Xu, M. Liang, S. Qi, W. Sun, L. Lv, F. Du, B. Wang, S. Chen, Y. Wang, Y. Yu, *ACS Nano* **2021**, *15*, 47–80.

[4] a) Y. Liang, P. Zhang, S. Yang, Z. Tao, J. Chen, *Adv. Energy Mater.* **2013**, *3*, 600–605; b) T. Ma, Q. Zhao, J. Wang, Z. Pan, J. Chen, *Angew. Chem. Int. Ed.* **2016**, *55*, 6428–6432; *Angew. Chem.* **2016**, *128*, 6538–6542.

[5] C. Peng, G. Ning, J. Su, G. Zhong, W. Tang, B. Tian, C. Su, D. Yu, L. Zu, J. Yang, M. Ng, Y. Hu, Y. Yang, M. Armand, K. P. Loh, *Nat. Energy* **2017**, *2*, 17074.

[6] Q. Deng, S. He, J. Pei, C. Fan, C. Li, B. Cao, Z.-H. Lu, J. Li, *Electrochem. Commun.* **2017**, *75*, 29–32.

[7] C. Luo, O. Borodin, X. Ji, S. Hou, K. J. Gaskell, X. Fan, J. Chen, T. Deng, R. Wang, J. Jiang, C. Wang, *Proc. Natl. Acad. Sci. USA* **2018**, *115*, 2004–2009.

[8] L. Li, Y. Yin, J. Hei, X. Wan, M. Li, Y. Cui, *Small* **2021**, *17*, 2005752.

[9] Y. Lu, Q. Zhang, L. Li, Z. Niu, J. Chen, *Chem* **2018**, *4*, 2786–2813.

[10] H. Li, M. Eddaoudi, M. O'Keeffe, O. M. Yaghi, *Nature* **1999**, *402*, 276–279.

[11] a) Z. Zhang, H. Yoshikawa, K. Awaga, *J. Am. Chem. Soc.* **2014**, *136*, 16112–16115; b) S. Xu, G. Wang, B. P. Biswal, M. Addicoat, S. Paasch, W. Sheng, X. Zhuang, E. Brunner, T. Heine, R. Berger, X. Feng, *Angew. Chem. Int. Ed.* **2019**, *58*, 849–853; *Angew. Chem.* **2019**, *131*, 859–863; c) Q. Jiang, P. Xiong, J. Liu, Z. Xie, Q. Wang, X. Q. Yang, E. Hu, Y. Cao, J. Sun, Y. Xu, L. Chen, *Angew. Chem. Int. Ed.* **2020**, *59*, 5273–5277; *Angew. Chem.* **2020**, *132*, 5311–5315; d) K. Wada, K. Sakaushi, S. Sasaki, H. Nishihara, *Angew. Chem. Int. Ed.* **2018**, *57*, 8886–8890; *Angew. Chem.* **2018**, *130*, 9024–9028.

[12] a) N. Lahiri, N. Lotfizadeh, R. Tsuchikawa, V. V. Deshpande, J. Louie, *J. Am. Chem. Soc.* **2017**, *139*, 19–22; b) M. S. Yao, X. J. Lv, Z. H. Fu, W. H. Li, W. H. Deng, G. D. Wu, G. Xu, *Angew. Chem. Int. Ed.* **2017**, *56*, 16510–16514; *Angew. Chem.* **2017**, *129*,

16737–16741; c) Y. Cui, J. Yan, Z. Chen, J. Zhang, Y. Zou, Y. Sun, W. Xu, D. Zhu, *Adv. Sci.* **2019**, *6*, 1802235; d) X. Huang, P. Sheng, Z. Y. Tu, F. J. Zhang, J. H. Wang, H. Geng, Y. Zou, C. A. Di, Y. P. Yi, Y. M. Sun, W. Xu, D. B. Zhu, *Nat. Commun.* **2015**, *6*, 8.

[13] J. Park, M. Lee, D. Feng, Z. Huang, A. C. Hinckley, A. Yakovenko, X. Zou, Y. Cui, Z. Bao, *J. Am. Chem. Soc.* **2018**, *140*, 10315–10323.

[14] C. Zhang, K. Fan, Y. Chen, Y. Wu, C. Wang, *ACS Appl. Electron. Mater.* **2021**, *3*, 1947–1958.

[15] J.-H. Dou, M. Q. Arguilla, Y. Luo, J. Li, W. Zhang, L. Sun, J. L. Mancuso, L. Yang, T. Chen, L. R. Parent, G. Skorupskii, N. J. Libretto, C. Sun, M. C. Yang, P. V. Dip, E. J. Brignole, J. T. Miller, J. Kong, C. H. Hendon, J. Sun, M. Dincă, *Nat. Mater.* **2021**, *20*, 222–228.

[16] a) Q. Yu, Z. Xue, M. Li, P. Qiu, C. Li, S. Wang, J. Yu, H. Nara, J. Na, Y. Yamauchi, *Adv. Energy Mater.* **2021**, *11*, 2002523; b) L. Kong, M. Liu, H. Huang, Y. Xu, X. Bu, *Adv. Energy Mater.* **2021**, *11*, 2100172.

[17] X. Han, G. Qing, J. Sun, T. Sun, *Angew. Chem. Int. Ed.* **2012**, *51*, 5147–5151; *Angew. Chem.* **2012**, *124*, 5237–5241.

[18] a) Z. Wang, G. Wang, H. Qi, M. Wang, M. Wang, S. Park, H. Wang, M. Yu, U. Kaiser, A. Fery, S. Zhou, R. Dong, X. Feng, *Chem. Sci.* **2020**, *11*, 7665–7671; b) L. Guo, J. Sun, W. Zhang, L. Hou, L. Liang, Y. Liu, C. Yuan, *ChemSusChem* **2019**, *12*, 5051–5058; c) K. W. Nam, S. S. Park, R. dos Reis, V. P. Dravid, H. Kim, C. A. Mirkin, J. F. Stoddart, *Nat. Commun.* **2019**, *10*, 4948.

[19] J. Liu, D. Yang, Y. Zhou, G. Zhang, G. Xing, Y. Liu, Y. Ma, O. Terasaki, S. Yang, L. Chen, *Angew. Chem. Int. Ed.* **2021**, *60*, 14473–14479; *Angew. Chem.* **2021**, *133*, 14594–14600.

[20] N. S. McIntyre, M. G. Cook, *Anal. Chem.* **1975**, *47*, 2208–2213.

[21] a) Q. Li, H. Li, Q. Xia, Z. Hu, Y. Zhu, S. Yan, C. Ge, Q. Zhang, X. Wang, X. Shang, S. Fan, Y. Long, L. Gu, G. X. Miao, G. Yu, J. S. Moodera, *Nat. Mater.* **2021**, *20*, 76–83; b) H. Kim, W. Choi, J. Yoon, J. H. Um, W. Lee, J. Kim, J. Cabana, W.-S. Yoon, *Chem. Rev.* **2020**, *120*, 6934–6976.

[22] H. Nagatomi, N. Yanai, T. Yamada, K. Shiraishi, N. Kimizuka, *Chem. Eur. J.* **2018**, *24*, 1806–1810.

[23] L. Wang, Y. Han, X. Feng, J. Zhou, P. Qi, B. Wang, *Coord. Chem. Rev.* **2016**, *307*, 361–381.

[24] Z. Wu, D. Adekoya, X. Huang, M. J. Kiefel, J. Xie, W. Xu, Q. Zhang, D. Zhu, S. Zhang, *ACS Nano* **2020**, *14*, 12016–12026.

[25] a) H. Jin, S. Xin, C. Chuang, W. Li, H. Wang, J. Zhu, H. Xie, T. Zhang, Y. Wan, Z. Qi, W. Yan, Y.-R. Lu, T.-S. Chan, X. Wu, J. B. Goodenough, H. Ji, X. Duan, *Science* **2020**, *370*, 192–197; b) J. Liu, Y. Zhang, L. Zhang, F. Xie, A. Vasileff, S.-Z. Qiao, *Adv. Mater.* **2019**, *31*, 1901261; c) Y. Xu, C. Zhang, M. Zhou, Q. Fu, C. Zhao, M. Wu, Y. Lei, *Nat. Commun.* **2018**, *9*, 1720.

[26] O. Buyukcakir, R. Yuksel, Y. Jiang, S. H. Lee, W. K. Seong, X. Chen, R. S. Ruoff, *Angew. Chem. Int. Ed.* **2019**, *58*, 872–876; *Angew. Chem.* **2019**, *131*, 882–886.

[27] Y. Lu, X. Hou, L. Miao, L. Li, R. Shi, L. Liu, J. Chen, *Angew. Chem. Int. Ed.* **2019**, *58*, 7020–7024; *Angew. Chem.* **2019**, *131*, 7094–7098.